

Paraxial Eikonal Solvers for Anisotropic Quasi-P Travel Times

Jianliang Qian and William W. Symes

Department of Computational and Applied Mathematics, Rice University, Houston, Texas 77251-1892

E-mail: jlqian@caam.rice.edu, symes@caam.rice.edu

Received August 2, 2000; revised April 13, 2001

The first-arrival quasi-P wave travel-time field in an anisotropic elastic solid solves a first-order nonlinear partial differential equation, the qP eikonal equation, which is a stationary Hamilton–Jacobi equation. The solution of the *paraxial* quasi-P eikonal equation, an evolution Hamilton–Jacobi equation in depth, gives the first-arrival travel time along downward propagating rays. We devise nonlinear numerical algorithms to compute the paraxial Hamiltonian for quasi-P wave propagation in general anisotropic media. A second-order essentially nonoscillatory (ENO) Runge–Kutta scheme solves this paraxial eikonal equation with a point source as an initial condition in $O(N)$ floating point operations, where N is the number of grid points. Numerical experiments using 2-D transversely isotropic models with inclined symmetry axes demonstrate the accuracy of the algorithms. © 2001 Academic Press

Key Words: Hamilton–Jacobi; viscosity solution; paraxial eikonal solvers; anisotropic travel time; weighted essentially nonoscillatory scheme (WENO).

1. INTRODUCTION

Travel-time computation plays a central role in many seismic data processing methods, such as Kirchhoff depth migration and tomographic velocity analysis. Since seismic wave propagation is anisotropic in many sedimentary rocks, maximal imaging resolution requires that travel-time computation honor anisotropy whenever it seriously affects data kinematics [6, 33, 48]. Among the travel times for various waves in anisotropic media, quasi-compressional (“quasi-P” or “qP”) wave travel times are considered most important [47, 48].

Based on the asymptotic methods for wave equations and geometrical optics [4, 19], the travel times satisfy so-called eikonal equations, a class of Hamilton–Jacobi equations. The eikonal equation can be solved by the method of characteristics [13], which constructs the characteristic curves called “rays.” The methods based on the characteristic equations are called “ray-tracing methods” [5, 32, 44], and they work for both *isotropic* and *anisotropic*

solids. But ray-tracing methods have some drawbacks. The nonuniform distribution of travel-time data from ray-tracing methods gives rise to cumbersome and expensive interpolations for application in seismic imaging. Therefore, many researchers appeal to finite-difference methods to solve the eikonal equation directly on regular Cartesian grids.

Finite-difference eikonal solvers compute the approximate first-arrival times directly on a prespecified grid, involve rather simple data structures, and are easy to code efficiently [21, 38, 40–43, 49, 50]. However, the methods cited describe only finite-difference travel-time algorithms for isotropic solids. Extension of these methods to anisotropic wave propagation is not entirely straightforward. Qin and Schuster [39] and Eaton [11] extended the expanding-wavefront scheme developed by Qin *et al.* [38] to the anisotropic medium, but their extensions work only for 2-D cases and have first-order accuracy only.

The finite-difference eikonal solvers cited above depend on the fact that for isotropic media the ray velocity vector, i.e., the *group velocity*, has the same direction as the travel-time gradient, i.e., the *phase velocity*, so that we can use the travel-time gradient as a reliable indicator of energy flow in extrapolating the travel-time field. However, this is no longer true for anisotropic media [10]. In [36], the authors established a reliable indicator of qP ray velocity direction by formulating a relation between the group velocity direction and the phase velocity direction; furthermore, they introduced a paraxial eikonal equation for quasi-P wave travel times, which is a Hamilton–Jacobi equation in evolution form. The goal of the current paper is to sketch theoretical formulations and present complete implementation details as well as illustrative applications of finite-difference methods for travel times of first-arriving qP waves in heterogeneous anisotropic solids.

The mathematical foundation of the finite-difference approach to travel-time computation comes from Lions’ [27] results pertaining to isotropic media: The first-arrival travel time is a particular generalized solution of the eikonal equation—the so-called viscosity solution—which is computable by finite-difference approximation [8].

The central hypothesis of this paper is that the first-arrival qP travel time is also a stable generalized solution and therefore computable by suitable finite-difference schemes. Also by analogy with the isotropic case, we expect so-called upwind schemes to be particularly successful in solving the paraxial eikonal equation with a point source as an initial condition [49]. Dellinger and Symes [9, 10] investigated this possibility but did not give full details of a workable algorithm. This paper applies a family of algorithms of the essentially nonoscillatory (ENO) type [30, 31] and weighted ENO (WENO) schemes [17, 28] to a depth-evolution (“paraxial”) form of the eikonal equation. The computed solution gives an accurate approximate time at every point of a Cartesian grid, which is connected to the source by a first-arriving ray whose velocity vector makes less than a prescribed angle with the vertical. A similar approach has proven quite successful for isotropic travel-time (and amplitude) computation for use in prestack modeling, migration, and inversion [12, 34, 46]. We expect similar applications for the algorithm presented here. There are other newly developed high-resolution schemes for Hamilton–Jacobi equations, such as central-difference schemes [24, 26], discontinuous Galerkin schemes [1, 15], and finite-volume schemes [22]; we plan to test these schemes on the eikonal equations in the seismic exploration setting in the near future. For examples of capturing multivalued travel times and caustics by solving Hamilton–Jacobi equations, see [2, 3].

We first summarize the eikonal equation for the quasi-P wave, which is the fastest propagating body wave; see [34, 36] for details. For down-going qP waves, the eikonal equation can be transformed to an evolution equation in depth, which we call the paraxial eikonal

equation. Definition of the paraxial eikonal depends on the relation of the aperture limitation, i.e., the indicator of the energy flow, defined in terms of the ray velocity vector and the travel-time gradient. However, due to the complexity of wave propagation in anisotropic solids, it is difficult to find an explicit form of the paraxial Hamiltonian. Therefore we have devised some numerical algorithms for computing the paraxial Hamiltonian. Since the theoretical results proved in [34, 36] are constructive, the design of the algorithms basically follows those constructions. A by-product of designing these algorithms is one that initializes the travel time in finite-difference schemes. Once the paraxial Hamiltonian is in place, we can use upwind finite-difference schemes to solve the paraxial eikonal equation. We use the ENO–Godunov family of finite-difference schemes [30, 31] to build qP eikonal solvers with arbitrary orders of accuracy, in two or three dimensions. Two-dimensional transversely isotropic examples illustrate the accuracy of the ENO/WENO schemes as well as the effect of the paraxial (aperture-limiting) assumption. In the Appendix, we present a new derivation of the first-order Godunov scheme which sheds light on how the upwind scheme works on the paraxial eikonal equation with a point source.

2. THE PARAXIAL EIKONAL EQUATION FOR QP WAVES

In a seismic exploration setting where velocity structures have mild lateral heterogeneity, most reflected wave energy propagates down to the target, then up to the surface. That is, the energy in such a wave field propagates along down-going rays: the x_3 (“z”) component of the ray velocity vector remains positive from source to target. The travel time along such down-going rays increases with depth and should be the solution of an evolution system in depth. This evolution system is the so-called paraxial eikonal equation for anisotropic media, which has been introduced by Qian and Symes [36].

High-frequency approximation to the elastic wave equation leads to the Christoffel equation [29, p. 84],

$$\sum_k \left(\sum_{i,l} a_{ijkl} p_i p_l - \delta_{jk} \right) U_k = 0, \quad (1)$$

in which a_{ijkl} are the components of the elastic tensor divided by density, U_k is the displacement vector for a particular asymptotic phase; $\mathbf{p} = \nabla \tau$ is the slowness vector; τ is the travel time or phase of the mode, and δ_{jk} is the Kronecker delta. Note that all these quantities depend on the spatial coordinate vector $\mathbf{x} = (x_1, x_2, x_3)$, though in this and some of the following displays this dependence has been suppressed for the sake of clarity. This equation has nontrivial solutions U_k only when

$$\det \left(\sum_{i,l} a_{ijkl} p_i p_l - \delta_{jk} \right) = 0. \quad (2)$$

Equation (2) is a sextic polynomial equation and characterizes the slowness surface which consists of three sheets corresponding to three wave modes. The three wave modes are quasi-P, quasi-SV, and quasi-SH, respectively [29]; see Fig. 1a.

The quasi-P slowness surface is strictly convex by the following argument [29, p. 92]. The slowness surface defined by Eq. (2) is sextic and consists of three sheets corresponding to three different waves. If the inner detached slowness sheet related to quasi-P waves is not

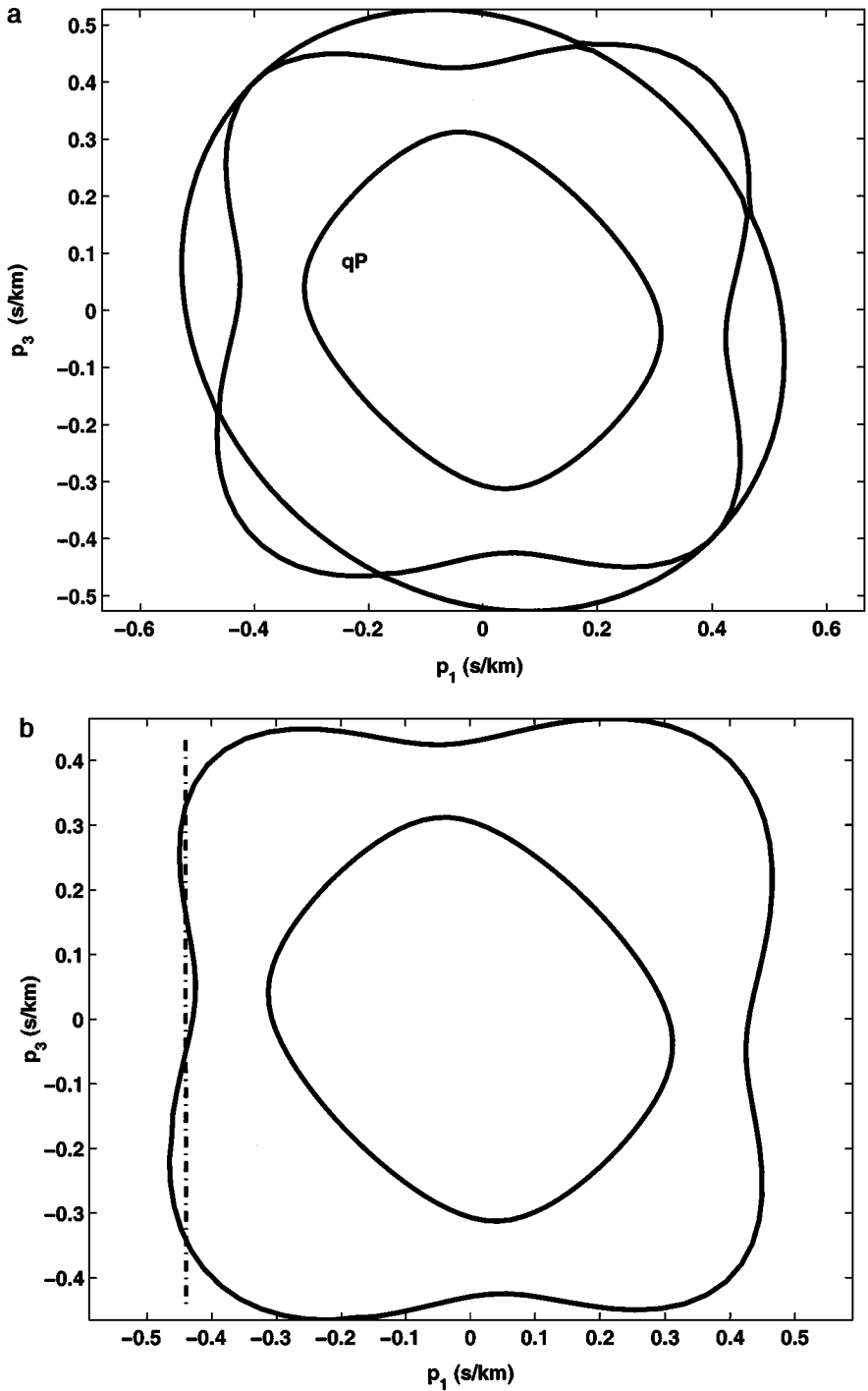


FIG. 1. The slowness surface for typical anisotropic media. (a) A sextic surface of three slowness sheets. (b) A quartic surface of two slowness sheets.

wholly strictly convex, a straight line could intersect the inner sheet at four or more points and yet make at least four further intersections with the remaining sheets; but any straight line must intersect the slowness surface at only six points, real or imaginary, because the slowness surface is sextic. By using the convexity of a quasi-P slowness surface, Qian and Symes [36] first introduced a function H to pick out the part of a quasi-P slowness surface which corresponds to the down-going rays and then modified the function H to obtain a paraxial Hamiltonian H_Δ , which is defined in the whole horizontal slowness space.

For convenience, we summarize the main results of [36] in the notation used in this paper; see also [34]. Assuming that the qP slowness surface is

$$S(\mathbf{x}, \mathbf{p}) = 1, \quad (3)$$

then

- For each \mathbf{x} and horizontal slowness vector (p_1, p_2) , because of the convexity of the slowness surface, there are at most two choices of p_3 for which $\mathbf{p} = (p_1, p_2, p_3)$ solves the slowness surface equation (3).
- When two distinct solutions exist, only one satisfies (see Fig. 2)

$$\frac{dx_3}{dt} = \frac{\partial S(\mathbf{x}, \mathbf{p})}{\partial p_3}(\mathbf{x}, \mathbf{p}) > 0,$$

which corresponds to the down-going rays.

- The above choice defines p_3 as a function of \mathbf{x}, p_1, p_2 ,

$$p_3 = H(\mathbf{x}, p_1, p_2), \quad (4)$$

where H is a concave Hamiltonian;

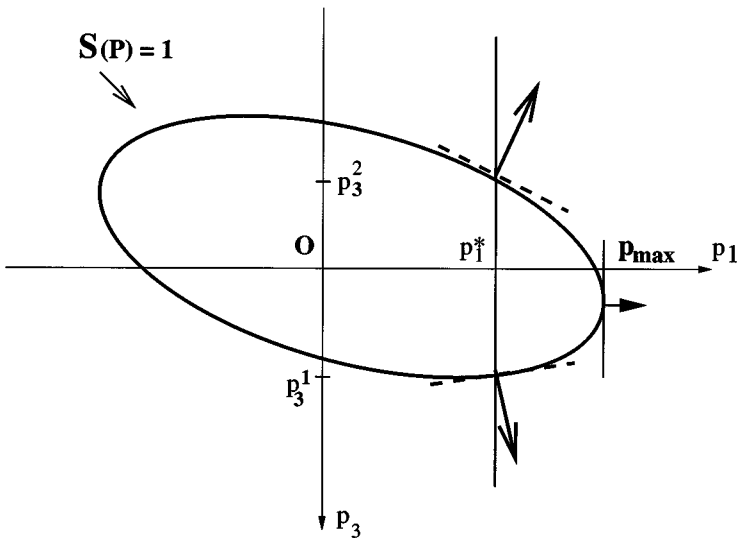


FIG. 2. The p_3 components of outward normals at the two intersections on the convex slowness surface have opposite signs.

• Parametrize the horizontal variables (p_1, p_2) by polar coordinates, $(p_1, p_2) = (p' \cos \phi, p' \sin \phi)$, where $p' = \sqrt{p_1^2 + p_2^2}$. For each planar angle ϕ , the family of planes with the outward normal $(\cos \phi, \sin \phi, 0)$ is tangent to the quasi-P slowness surface at exactly one point

$$(p_1(\phi), p_2(\phi), p_3(\phi)) = (p'_{\max}(\phi) \cos \phi, p'_{\max}(\phi) \sin \phi, p_3(\phi)), \quad (5)$$

where $p'_{\max} = \sqrt{p_1^2(\phi) + p_2^2(\phi)}$ (see Fig. 2).

• Choosing the paraxial parameter $0 < \Delta < 1$, define function H_Δ as

$$H_\Delta(p_1, p_2) = \begin{cases} H(p_1, p_2), & \text{if } p' \leq (1 - \Delta)p'_{\max}(\phi); \\ H((1 - \Delta)p'_{\max}(\phi) \cos \phi, (1 - \Delta)p'_{\max}(\phi) \sin \phi), & \text{else} \end{cases} \quad (6)$$

here H_Δ remains a concave Hamiltonian.

• The *paraxial eikonal equation* is

$$\frac{\partial \tau}{\partial x_3} = H_\Delta \left(\mathbf{x}, \frac{\partial \tau}{\partial x_1}, \frac{\partial \tau}{\partial x_2} \right). \quad (7)$$

Because the largest eigenvalue of the Christoffel matrix $\sum_{i,l} a_{ijkl} p_i p_l$ is simple [14, p. 95], which corresponds to the quasi-P wave mode, it depends smoothly on the slowness vector \mathbf{p} and the elastic tensor. Therefore, the above paraxial Hamiltonian H_Δ is continuous. The concavity of the Hamiltonian H follows from its definition because it is based on a function defined by the graph corresponding to the down-going part of the slowness surface; see [34] for a rigorous proof.

The paraxial parameter Δ is used to limit the slowness vector, which in turn imposes an implicit restriction on the group velocity vector thanks to the strict convexity of the quasi-P slowness surface [34]. Because the mapping from the slowness vector to the group velocity vector is explicit, the above construction leads to an efficient algorithm and the resultant Hamiltonian has a built-in reliable indicator of the group velocity direction. In [20], the local convexity of wavefronts in transversely isotropic media is used to extrapolate the travel-time field. However, the framework presented here can be applied to arbitrary anisotropic media to obtain the quasi-P travel-time field.

In some special cases, we can find explicit forms for H_Δ , such as in isotropic media and transversely isotropic media with vertical symmetry axes (VTI); for examples, see [36]. In general, since the related eigenvalue problem has no closed-form solution, it is difficult to obtain an explicit form for H_Δ .

3. COMPUTING THE PARAXIAL HAMILTONIAN H_Δ

The slowness surface equation (2) is a sextic polynomial equation in p_i ($i = 1, 2, 3$), which characterizes three wave modes; that is, the slowness surface is sextic and consists of three sheets (see Fig. 1). The inner sheet is convex and corresponds to the quasi-P wave mode. By introducing the planar polar coordinates, we have transformed this sextic polynomial equation into a sextic polynomial equation in p' and p_3 for each planar angle ϕ ; hence, we now have a two-dimensional problem. In the following development of algorithms,

we concentrate on the numerical construction of a paraxial quasi-P Hamiltonian for two-dimensional general anisotropic media.

Suppose that the two-dimensional slowness surface is given by

$$F(p_1, p_3) = 0, \tag{8}$$

where F is a sextic or quartic polynomial in p_1 and p_3 , respectively. The sextic case corresponds to three linked wave modes, namely, quasi-P and two other wave modes; see Fig. 1a. The quartic case corresponds to two coupled wave modes, namely, quasi-P and one transverse wave mode; see Fig. 1b. Specifically, in this section we assume that F is a sextic polynomial in p_1 and p_3 ; the quartic case can be treated similarly.

For arbitrary p_1^* , there are four possibilities for the roots p_3 of the sextic polynomial equation $F(p_1^*, p_3) = 0$: (1) no real roots at all; (2) two real roots; (3) four real roots; and (4) six real roots. We are especially interested in case (4) since this means that among the six real roots there are two roots *possibly* corresponding to the quasi-P wave. Because the quasi-P slowness surface, denoted \mathbf{S} , is convex and separated from and nested inside two other ovoid surfaces, the straight line $p_1 = p_1^*$ has two intersection points with \mathbf{S} if $(p_1 = p_1^*, 0)$ is inside the domain enclosed by the quasi-P slowness surface. This *if* condition is important because it is possible that no roots among the six real roots correspond to the quasi-P wave; see the dashed line in Fig. 1b, which corresponds to cusps. Since the origin is in the domain enclosed by \mathbf{S} , p_1^* can be taken small enough to guarantee that the straight line $p_1 = p_1^*$ has six real intersection points with the slowness surface, among which two are on the quasi-P slowness surface \mathbf{S} . The six real roots can be sorted into ascending order; moreover, the third and fourth roots correspond to the two intersection points with the quasi-P slowness surface, denoted as p_3^{up} and p_3^{dn} .

Because \mathbf{S} is strictly convex and closed, there are two extreme points at which $F = 0$ and $\frac{\partial F}{\partial p_3} = 0$; by the method of characteristics,

$$\begin{aligned} \frac{dx_1}{dt} &= v_g^1 = \left(p_1 \frac{\partial F}{\partial p_1} + p_3 \frac{\partial F}{\partial p_3} \right)^{-1} \frac{\partial F}{\partial p_1}, \\ \frac{dx_3}{dt} &= v_g^3 = \left(p_1 \frac{\partial F}{\partial p_1} + p_3 \frac{\partial F}{\partial p_3} \right)^{-1} \frac{\partial F}{\partial p_3}, \end{aligned} \tag{9}$$

they correspond to the two horizontal rays (pointing to the positive and negative x_1 -directions). To locate such points, we need two sets of intersection points (p_1^*, p_3^{up}) and (p_1^*, p_3^{dn}) , which can be computed with p_1^* chosen as positive and negative numbers near zero, respectively.

Assuming that (p_1^*, p_3^{up}) and (p_1^*, p_3^{dn}) on the quasi-P slowness surface \mathbf{S} are known, we can find on \mathbf{S} an extreme point $(p_1^{\text{m}}, p_3^{\text{m}})$ which corresponds to the stationary point of function $p_1 = f(p_3)$ defined by the graph $\{(p_1, p_3) : p_1 \geq p_1^* > 0, p_3^{\text{dn}} \leq p_3 \leq p_3^{\text{up}}, F(p_1, p_3) = 0\}$; see Fig. 2. Since the function f is convex, its derivative is monotonic; therefore, a typical nonlinear iterative solver can be used to compute the unique stationary point, such as the Newton method. The above stationary point is also of critical importance in the adaptation of upwind finite-difference schemes from numerical methods for Hamilton–Jacobi equations, because in that setting it is called the sonic point and is needed to decide the upwinding direction.

Once the two extreme points (p_1^+, p_3^+) and (p_1^-, p_3^-) corresponding to the two horizontal rays are located, it is easy to see that all $p_1 \in ((1 - \Delta)p_1^-, (1 - \Delta)p_1^+)$ give rise to down-going and up-going quasi-P rays by utilizing different roots of p_3 , where Δ is the user-specified paraxial parameter for depth direction marching. For $p_1 \leq (1 - \Delta)p_1^-$, we simply set the paraxial Hamiltonian $H_\Delta(p_1) = H((1 - \Delta)p_1^-)$; similar treatment is given to $p_1 \geq (1 - \Delta)p_1^+$.

Supposing that we have two extreme points (p_1^+, p_3^+) and (p_1^-, p_3^-) , the ray tracing equation says that the outward normals at these two extreme points correspond to the rays which point to the horizontal directions. Knowing this, we can design a shooting method to compute the travel time from a source point to a specific point in homogeneous anisotropic media. Since the group angle is known, the goal is to find the corresponding slowness vector to give the correct group angle. The following results.

ALGORITHM 1:

- Input: (x_1^s, z_1^s) , (x_1^o, z_1^o) , (p_1^+, p_3^+) , and (p_1^-, p_3^-) .
- Set $p_1^a \leftarrow p_1^-$ and $p_1^b \leftarrow p_1^+$.
- Compute: $p_1^c \leftarrow \frac{1}{2}(p_1^a + p_1^b)$.
- Compute: $\text{gcos} \leftarrow \frac{x_1^o - x_1^s}{\sqrt{(x_1^o - x_1^s)^2 + (z_1^o - z_1^s)^2}}$.
- While $p_1^a < p_1^c$ and $p_1^c < p_1^b$, do
 - $\text{root_}p_3 \leftarrow$ all roots of $F(p_1^c, p_3) = 0.0$.
 - Sort the roots in ascending order: $\text{root_}p_3 \leftarrow \text{sort}(\text{root_}p_3)$.
 - Pick out the one for down-going qP wave:
 - * if F is sextic: $p_3^c \leftarrow \text{root_}p_3(4)$.
 - * if F is quartic: $p_3^c \leftarrow \text{root_}p_3(3)$.
 - Compute the group velocity vector (v_g^1, v_g^3) at (p_1^c, p_3^c) by Eqs. (9).
 - Compute: $\text{gvel} \leftarrow \frac{v_g^1}{\sqrt{(v_g^1)^2 + (v_g^3)^2}}$.
 - If $\text{gvel} \geq \text{gcos}$, then $p_1^b \leftarrow p_1^c$ and $p_1^c \leftarrow 0.5(p_1^a + p_1^b)$; else $p_1^a \leftarrow p_1^c$ and $p_1^c \leftarrow 0.5(p_1^a + p_1^b)$.
- Compute travel time: $t = \frac{\sqrt{(x_1^o - x_1^s)^2 + (z_1^o - z_1^s)^2}}{\sqrt{(v_g^1)^2 + (v_g^3)^2}}$.

Algorithm 1 is useful for initializing the travel time to start the finite-difference schemes.

4. ENO AND WENO FOR PARAXIAL EIKONAL EQUATIONS

Equation (7) is a nonlinear first-order PDE for travel time τ . However, the travel time is not unique: when the elastic parameters vary with position, in general many rays pass over at least some points in the subsurface so that the travel-time field is multivalued [2]. One choice of unique travel time for each subsurface point is the *least time* (“first-arrival time”). It turns out that for isotropic media this first-arrival travel-time field is the *viscosity solution* of the eikonal equation [27]; we surmise that this is also true for anisotropic problems with a convex slowness surface. Qian and Symes [36] proved that the Hamiltonian of the quasi-P paraxial eikonal equation is concave, so its (unbounded) viscosity solution exists and is unique [7, 16, 23, 26]; furthermore, upwind schemes can be used to compute this viscosity solution successfully [8].

To compute the first-arrival travel-time field with a grid-based finite-difference scheme, we derived a first-order upwind scheme from ray tracing rather than directly from the eikonal equation; see the Appendix. We use this first-order scheme as a building block for

designing high-order schemes. To increase the order of convergence, we employ higher order essentially nonoscillatory and weighted ENO refinements. ENO schemes were introduced by Osher and Sethian [30] and Osher and Shu [31] as a means for solving Hamilton–Jacobi equations. WENO schemes were first proposed by Liu, *et al.* [28] as a means to overcome the drawbacks of ENOs. Jiang and Peng [17] made further improvements and extensions for Hamilton–Jacobi equations. Because WENO schemes are extensions of ENO schemes, we present second-order ENO schemes first.

Given mesh sizes Δx_1 , Δx_2 , and Δx_3 , we denote by $\tau_{m,k}^n$ by the numerical approximation of the viscosity solution $\tau(x_1^m, x_2^k, x_3^n)$ of Eq. (7) at the grid point (x_1^m, x_2^k, x_3^n) . Define the backward (−) and forward (+) first-order difference quotient approximations of the left and right derivatives of $\tau(x_1, x_2, x_3)$ at the location (x_1^m, x_2^k, x_3^n) with respect to x_1 and x_2 as

$$D_{x_1}^\pm \tau_{m,k}^n = \pm \frac{\tau_{m\pm 1,k}^n - \tau_{m,k}^n}{\Delta x_1}, \quad D_{x_2}^\pm \tau_{m,k}^n = \pm \frac{\tau_{m,k\pm 1}^n - \tau_{m,k}^n}{\Delta x_2}. \tag{10}$$

The second-order ENO refinements to $\frac{\partial \tau}{\partial x_1}$ [30] are

$$D_{x_1}^{\pm,2} \tau_{m,k}^n = D_{x_1}^\pm \tau_{m,k}^n \mp \frac{1}{2} \Delta x_1 m (D_{x_1}^\pm D_{x_1}^\pm \tau_{m,k}^n, D_{x_1}^- D_{x_1}^+ \tau_{m,k}^n), \tag{11}$$

with

$$m(x, y) = \min(\max(x, 0), \max(y, 0)) + \max(\min(x, 0), \min(y, 0)). \tag{12}$$

ENO refinements for $\frac{\partial \tau}{\partial x_2}$ are defined similarly.

So a second-order ENO Runge–Kutta scheme for Eq. (7) can be formulated as

$$\begin{aligned} \tau_{m,k}^{n+\frac{1}{2}} &= \tau_{m,k}^n + \Delta x_3^{\text{cfl}} \hat{H}_\Delta (D_{x_1}^{+,2} \tau_{m,k}^n, D_{x_1}^{-,2} \tau_{m,k}^n, D_{x_2}^{+,2} \tau_{m,k}^n, D_{x_2}^{-,2} \tau_{m,k}^n), \\ \tau_{m,k}^{n+1} &= \frac{1}{2} \left(\tau_{m,k}^n + \tau_{m,k}^{n+\frac{1}{2}} + \Delta x_3^{\text{cfl}} \hat{H}_\Delta \left(D_{x_1}^{+,2} \tau_{m,k}^{n+\frac{1}{2}}, D_{x_1}^{-,2} \tau_{m,k}^{n+\frac{1}{2}}, D_{x_2}^{+,2} \tau_{m,k}^{n+\frac{1}{2}}, D_{x_2}^{-,2} \tau_{m,k}^{n+\frac{1}{2}} \right) \right), \end{aligned}$$

where the flux \hat{H}_Δ is defined by [31]

$$\hat{H}_\Delta(u^+, u^-, v^+, v^-) = \text{ext}_{u \in I(u^-, u^+)} \text{ext}_{v \in I(v^-, v^+)} H_\Delta(u, v). \tag{13}$$

The function $\text{ext}_{u \in I(a,b)} = \max_{a \leq u \leq b}$ if $a \leq b$, $\text{ext}_{u \in I(a,b)} = \min_{b \leq u \leq a}$ else; $I(a, b) = [\min(a, b), \max(a, b)]$; Δx_3^{cfl} is the Courant–Friedrichs–Lewy (“CFL”) step,

$$\Delta x_3^{\text{cfl}} \left(\max_{p_1, p_2} \sqrt{\left(\frac{\partial H_\Delta}{\partial p_1} \right)^2 + \left(\frac{\partial H_\Delta}{\partial p_2} \right)^2} \right) \leq \frac{\Delta x_1 \Delta x_2}{\sqrt{\Delta x_1^2 + \Delta x_2^2}}, \tag{14}$$

with the maximum taken over the relevant range of p_1 and p_2 . Since H_Δ is concave [36], Inequality (14) reduces to

$$\Delta x_3^{\text{cfl}} \left(\max_{\{(p_1^\phi, p_2^\phi) : 0 \leq \phi \leq 2\pi\}} \sqrt{\left(\frac{\partial H_\Delta}{\partial p_1} \right)^2 + \left(\frac{\partial H_\Delta}{\partial p_2} \right)^2} \right) \leq \frac{\Delta x_1 \Delta x_2}{\sqrt{\Delta x_1^2 + \Delta x_2^2}}, \tag{15}$$

where $(p_1^\phi, p_2^\phi) = ((1 - \Delta)p_{\max}(\phi) \cos \phi, (1 - \Delta)p_{\max}(\phi) \sin \phi)$.

Using the concavity of the Hamiltonian H_Δ , the above flux function \hat{H}_Δ is not difficult to compute as long as the ‘‘sonic point’’ (at which $\frac{\partial H_\Delta}{\partial p_1}$ or $\frac{\partial H_\Delta}{\partial p_2}$ changes sign) is located. To locate sonic points, we can use the algorithms for the extreme points explained above. If the sonic point is at $p_1 = 0$ or $p_2 = 0$, which is true for the isotropic eikonal equation and the eikonal equation for the transversely isotropic medium with a vertical symmetry axis, we can simplify the above scheme,

$$\tau_{m,k}^{n+\frac{1}{2}} = \tau_{m,k}^n + \Delta x_3^{\text{cfl}} H_\Delta \left(\left(\frac{\partial \tau}{\partial x_1} \right)_{m,k}^n, \left(\frac{\partial \tau}{\partial x_2} \right)_{m,k}^n \right), \quad (16)$$

$$\tau_{m,k}^{n+1} = \frac{1}{2} \left(\tau_{m,k}^n + \tau_{m,k}^{n+\frac{1}{2}} + \Delta x_3^{\text{cfl}} H_\Delta \left(\left(\frac{\partial \tau}{\partial x_1} \right)_{m,k}^{n+\frac{1}{2}}, \left(\frac{\partial \tau}{\partial x_2} \right)_{m,k}^{n+\frac{1}{2}} \right) \right), \quad (17)$$

where

$$\left(\frac{\partial \tau}{\partial x_1} \right)_{m,k}^n = \text{maxmod}(\max(D_{x_1}^{-,2} \tau_m^n, 0), \min(D_{x_1}^{+,2} \tau_m^n, 0)), \quad (18)$$

$$\left(\frac{\partial \tau}{\partial x_2} \right)_{m,k}^n = \text{maxmod}(\max(D_{x_2}^{-,2} \tau_m^n, 0), \min(D_{x_2}^{+,2} \tau_m^n, 0)), \quad (19)$$

with maxmod returning the larger value in modulus; see [21, 35, 36].

In the upwind framework, second-order ENO schemes diminish total variation, hence they have at least subsequences which converge to weak solutions [25, 45]. There is no known convergence result for ENO schemes of orders higher than 2, even for smooth solutions [45]. However, Jiang and Shu [18] proved that WENO schemes converge for smooth solutions. The main advantage of WENO schemes is that they provide smooth flux functions, so they are less sensitive to zeros of solutions and derivatives than ENO schemes.

The WENO second-order schemes for $D_{x_1}^\pm \tau_{m,k}$ are [17]

$$D_{x_1}^{-\text{W},2} \tau_{m,k} = \frac{1}{2} (D_{x_1}^+ \tau_{m-1,k} + D_{x_1}^+ \tau_{m,k}) - \frac{w_-}{2} (D_{x_1}^+ \tau_{m-2,k} - 2D_{x_1}^+ \tau_{m-1,k} + D_{x_1}^+ \tau_{m,k}), \quad (20)$$

$$D_{x_1}^{+\text{W},2} \tau_{m,k} = \frac{1}{2} (D_{x_1}^+ \tau_{m-1,k} + D_{x_1}^+ \tau_{m,k}) - \frac{w_+}{2} (D_{x_1}^+ \tau_{m+1,k} - 2D_{x_1}^+ \tau_{m,k} + D_{x_1}^+ \tau_{m-1,k}), \quad (21)$$

where

$$w_- = \frac{1}{1 + 2r_-^2}, \quad r_- = \frac{\delta + (D_{x_1}^- D_{x_1}^- \tau_{m,k})^2}{\delta + (D_{x_1}^- D_{x_1}^+ \tau_{m,k})^2}, \quad (22)$$

$$w_+ = \frac{1}{1 + 2r_+^2}, \quad r_+ = \frac{\delta + (D_{x_1}^+ D_{x_1}^+ \tau_{m,k})^2}{\delta + (D_{x_1}^+ D_{x_1}^- \tau_{m,k})^2}. \quad (23)$$

In the denominators of Eqs. (22) and (23), the small positive number δ is added to avoid dividing by zero. The WENO second-order schemes for $D_{x_2}^\pm \tau_{m,k}$ are defined similarly.

5. APPLICATION: INCLINED TI MEDIA

Although a general anisotropic solid has 21 independent elastic parameters, the transversely isotropic (TI) solid has only five independent elastic parameters. But it has, nevertheless, the essential anisotropic features we want to capture; therefore it is convenient to use TI solids as models to illustrate how the approaches work. First we consider the simplest case for TI solids, i.e., TI solids with vertical symmetry axes. Then we construct inclined TI models by rotating VTI models [20]. Because the slowness surface equation for the inclined TI model is a sextic polynomial equation which has the essential features of a general sextic slowness surface and admits no explicit solutions, it is suitable to use the model to test the proposed algorithms.

The elastic modulus matrix for transversely isotropic media with vertical symmetry axes (VTI) has 5 independent components among 12 nonzero components [29, 47]. A closed-form solution exists in this case for the eigenvalue problem (2). The quasi-P and quasi-SV slowness surface for VTI can be represented as a quartic polynomial equation (where the quasi-SH slowness surface is decoupled from the whole slowness surface),

$$G(q_1, q_3) \equiv aq_1^4 + bq_1^2q_3^2 + cq_3^4 + dq_1^2 + eq_3^2 + 1 = 0, \quad (24)$$

where

$$\begin{aligned} a &\equiv a_{11}a_{44}, \\ b &\equiv a_{11}a_{33} + a_{44}^2 - (a_{13} + a_{44})^2, \\ c &\equiv a_{33}a_{44}, \\ d &\equiv -(a_{11} + a_{44}), \\ e &\equiv -(a_{33} + a_{44}). \end{aligned}$$

In the above formulae, the Voigt recipe is assumed to simplify the elasticity tensor a_{ijkl} to obtain a_{ij} [47].

Rotate oq_1q_2 axes by angle ψ ,

$$q_1 = t_{11}p_1 + t_{13}p_3, \quad q_3 = t_{31}p_1 + t_{33}p_3,$$

where $t_{11} = t_{33} = \cos \psi$, $t_{13} = -t_{31} = \sin \psi$. Substituting the above relation into Eq. (24), we have a quartic polynomial equation in variables p_1, p_3 ,

$$\begin{aligned} F(p_1, p_3) &\equiv w_1p_1^4 + w_2p_1^3p_3 + w_3p_1^2p_3^2 + w_4p_1p_3^3 + w_5p_3^4 \\ &\quad + w_6p_1^2 + w_7p_1p_3 + w_8p_3^2 + w_9 = 0, \end{aligned} \quad (25)$$

where

$$\begin{aligned} w_1 &\equiv at_{11}^4 + bt_{11}^2t_{31}^2 + ct_{31}^4, \\ w_2 &\equiv 4at_{11}^3t_{13} + 2b(t_{11}^2t_{31}t_{33} + t_{11}t_{13}t_{31}^2) + 4ct_{31}^3t_{33}, \\ w_3 &\equiv 6at_{11}^2t_{13}^2 + b(t_{11}^2t_{33}^2 + 4t_{11}t_{13}t_{31}t_{33} + t_{13}^2t_{31}^2) + 6ct_{31}^2t_{33}^2, \end{aligned}$$

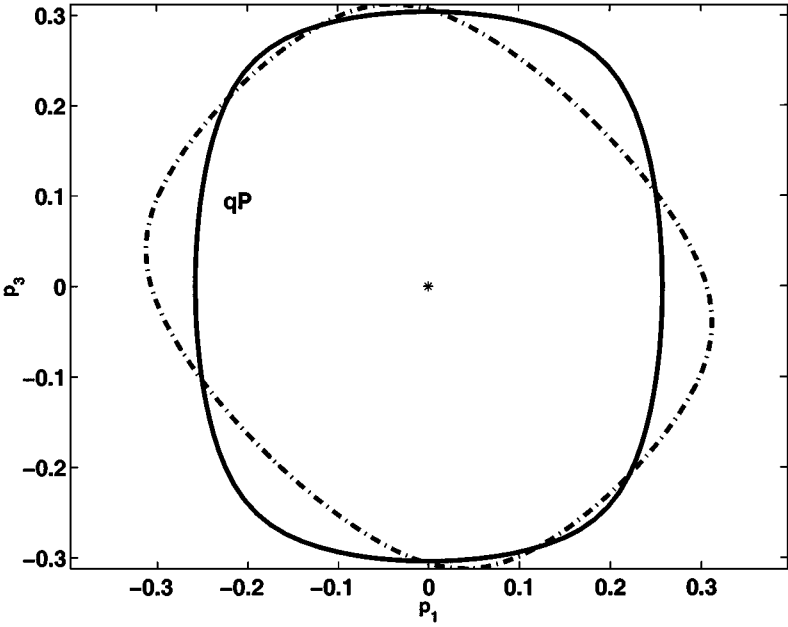


FIG. 3. The quasi-P slowness surface: unrotated (solid line) and after a rotation of 45° (dashed line).

$$\begin{aligned}
 w_4 &\equiv 4at_{11}t_{13}^3 + 2b(t_{11}t_{13}t_{33}^2 + t_{13}^2t_{31}t_{33}) + 4ct_{31}t_{33}^3, \\
 w_5 &\equiv at_{13}^4 + bt_{13}^2t_{33}^2 + ct_{33}^4, \\
 w_6 &\equiv dt_{11}^2 + et_{31}^2, \\
 w_7 &\equiv 2dt_{11}t_{13} + 2et_{31}t_{33}, \\
 w_8 &\equiv dt_{13}^2 + et_{33}^2, \\
 w_9 &\equiv 1.
 \end{aligned}$$

The two partial derivatives are given by

$$\begin{aligned}
 \frac{\partial F}{\partial p_1} &= 4w_1p_1^3 + 3w_2p_3p_1^2 + 2(w_3p_3^2 + w_6)p_1 + (w_4p_3^2 + w_7)p_3, \\
 \frac{\partial F}{\partial p_3} &= 4w_5p_3^3 + 3w_4p_1p_3^2 + 2(w_3p_1^2 + w_8)p_3 + (w_2p_1^2 + w_7)p_1.
 \end{aligned}$$

Figure 3 shows an original TI quasi-P slowness surface with a vertical symmetry axis and its rotated version.

6. NUMERICAL EXAMPLES

We have designed algorithms to be used for general anisotropic solids. In this section we test these algorithms on the inclined TI solids. We compute the paraxial Hamiltonian by using the idea explained above and solve the paraxial eikonal equation (7) by second-order ENO and WENO schemes. All examples are assumed to be of constant density.

In typical seismic exploration applications, the initial condition of the eikonal equation is given as a point source; thus the solution of the corresponding eikonal equation is called the fundamental solution with one-point singularity at the source [23]. Due to this singularity of the travel-time field which leads to the contamination of global numerical accuracy, we must use special techniques, such as the adaptive grid method [34, 35] or local uniform mesh refinement [21], to initialize the travel time. However, here we assume a homogeneous layer near the source (for which it is supposed to be easy to assign an accurate travel time) and start the finite-difference scheme some distance away from the source; namely, we use Algorithm 1 to compute the group velocity and directly initialize the travel time at every grid point on a surface away from the source. To solve the polynomial equation, we use MATLAB toolboxes; to locate the extreme points, we use Newton methods.

The example occupies the rectangle $\{-0.5 \text{ km} \leq x_1 \leq 0.5 \text{ km}, 0 \leq x_3 \leq 1 \text{ km}\}$; the source is located at $x_1 = 0.0 \text{ km}$, $x_3 = 0.0 \text{ km}$. The four elastic parameters of Zinc [29, p. 280] are $a_{11} = 15.90$, $a_{33} = 6.21$, $a_{13} = 4.82$, and $a_{44} = 4.00$; they can be transformed into Thomsen's parameters [47]: $\alpha_0 = 2.492 \text{ km/s}$, $\beta_0 = 2.00 \text{ km/s}$, $\epsilon = 0.7802$, and $\delta = 2.6562$.

According to the notion of Thomsen's weak anisotropy, these parameters show that the anisotropy is strong rather than weak. Therefore, this model will serve as an assay for the algorithms developed here and will be examined systematically. To do this, we will apply both ENO and WENO second-order schemes to both unrotated and rotated models.

To obtain an ITI model from the VTI model, the rotation angle ψ is 36 degrees. The initial data depth is at $x_3 = 0.04 \text{ km}$; that is, the initial data for the finite-difference scheme are given at this depth by Algorithm 1. The paraxial parameter Δ is taken as 0.01. In Tables I–IV Abs.Err is the maximum absolute error and Rel.Err is the maximum relative error, both measured at bottom $x_3 = 1 \text{ km}$. α is the estimated convergence order, where we use the travel time from Algorithm 1 as the exact solution to calibrate the travel time from the finite-difference scheme. The mathematical definitions of these three quantities are

$$\begin{aligned} \text{Abs.Err}(\tau, \Delta x_1) &= \max |\tau_{ana} - \tau_{fd}^{\Delta x_1}|, \\ \text{Rel.Err}(\tau, \Delta x_1) &= \frac{\max |\tau_{ana} - \tau_{fd}^{\Delta x_1}|}{\max |\tau_{ana}|}, \end{aligned}$$

and

$$\alpha = \frac{1}{\log 2} \log \left(\frac{\text{Rel.Err}(\tau, 2\Delta x_1)}{\text{Rel.Err}(\tau, \Delta x_1)} \right),$$

where τ_{ana} denotes the travel time by Algorithm 1 and τ_{fd} the travel time from the finite-difference scheme.

The results for VTI models are shown in Tables I and II. Table I shows that the convergence order α of the ENO scheme is going to 2 as Δx_1 goes to zero, while Table II shows that on average the second-order WENO scheme has a convergence order greater than 2.

Tables III and IV show the results for ITI models. The second-order ENO scheme does converge as a second-order scheme and it has stable error behaviors. The WENO second-order scheme seems to converge to a third-order scheme, which is consistent with the original construction of the WENO schemes [17].

Figure 4a shows the slowness surface for Zinc with a vertical symmetry axis, and Fig. 4b shows the slowness surface after it has been rotated 30 degrees. To generate

TABLE I
Convergence Order of ENO: VTI Model

Δx_1	Abs.Err(τ , Δx_1)(s)	Rel.Err(τ , Δx_1)	α
0.04	2.3589e-04	5.7583e-04	
0.02	1.0056e-04	2.4548e-04	1.2301
0.01	3.1957e-05	7.8011e-05	1.6539
0.005	9.1562e-06	2.2351e-05	1.8033
0.0025	2.4494e-06	5.9793e-06	1.9023

TABLE II
Convergence Order of WENO: VTI Model

Δx_1	Abs.Err(τ , Δx_1)(s)	Rel.Err(τ , Δx_1)	α
0.04	1.9809e-04	4.8553e-04	
0.02	7.0328e-06	1.7168e-05	4.8159
0.01	2.7634e-06	6.7457e-06	1.3477
0.005	5.1313e-07	1.2526e-06	2.4290
0.0025	8.2154e-08	2.0055e-07	2.6429

TABLE III
Convergence Order of ENO: ITI Model

Δx_1	Abs.Err(τ , Δx_1)(s)	Rel.Err(τ , Δx_1)	α
0.04	0.0022	0.0049	
0.02	6.8005e-04	0.0015	1.6938
0.01	1.8129e-04	4.0871e-04	1.9073
0.005	4.5921e-05	1.0353e-04	1.9811
0.0025	1.1749e-05	2.6489e-05	1.9666

TABLE IV
Convergence Order of WENO: ITI Model

Δx_1	Abs.Err(τ , Δx_1)(s)	Rel.Err(τ , Δx_1)	α
0.04	0.0017	0.0039	
0.02	4.4201e-04	9.9652e-04	1.9434
0.01	8.1029e-05	1.8268e-04	2.4476
0.005	1.0109e-05	2.2792e-05	3.0028
0.0025	1.2716e-06	2.8669e-06	2.9909

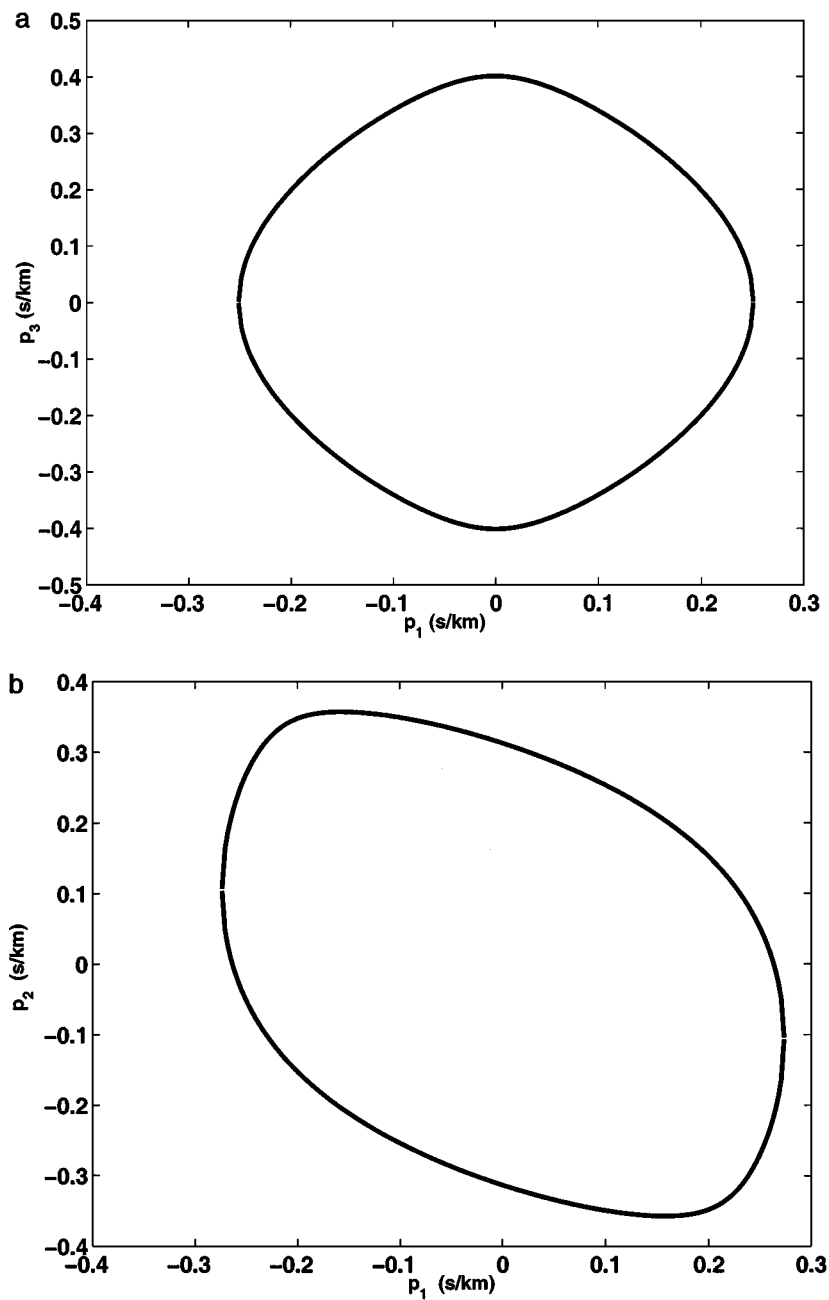


FIG. 4. The 2-D homogeneous Zinc model. (a) The original VTI slowness surface. (b) The inclined slowness surface with a rotation angle of 30° . The two slowness surfaces are generated by sampling an interval of p_1 in (p_1^-, p_1^+) .

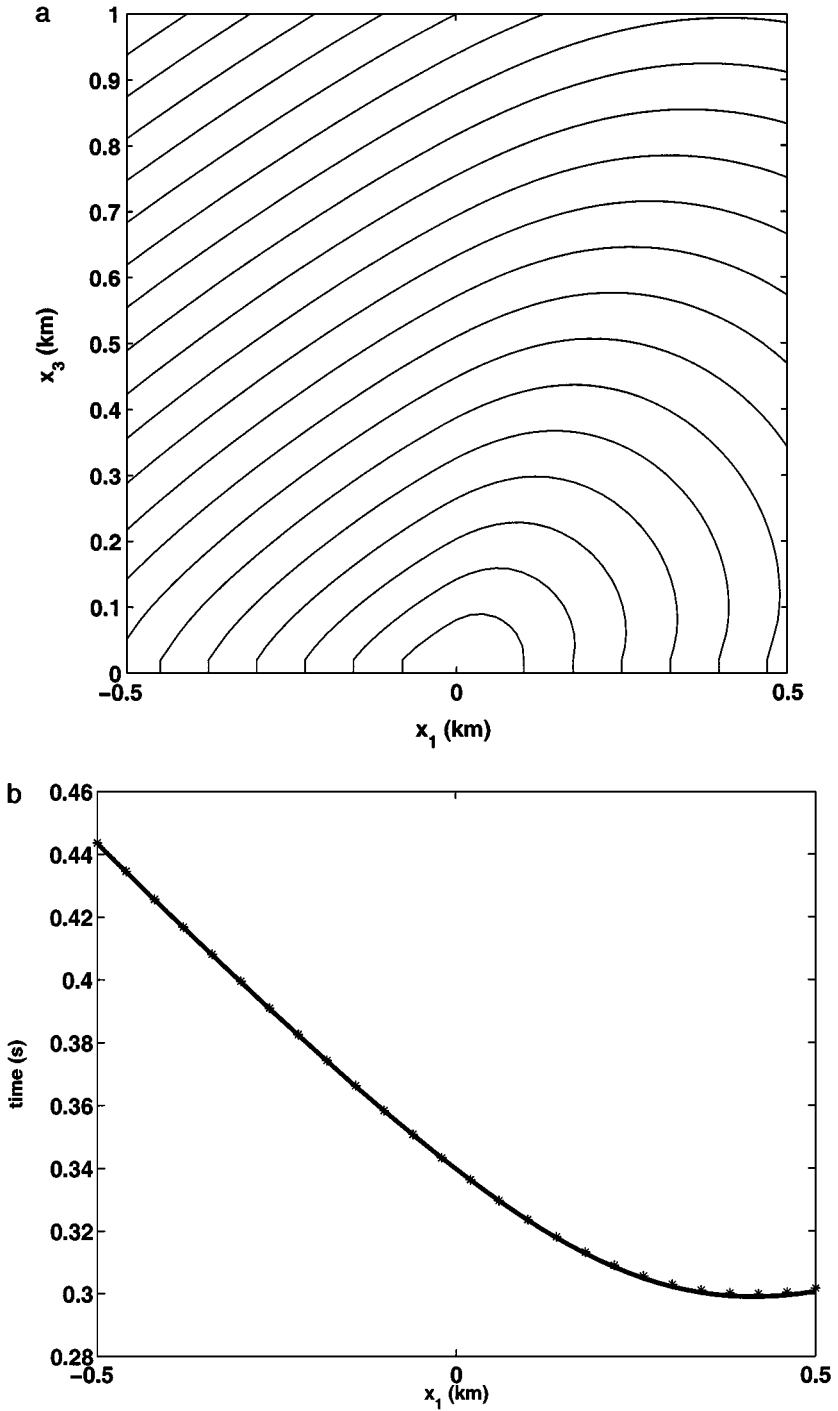


FIG. 5. The 2-D homogeneous inclined (36°) TI Zinc model with a second-order ENO scheme. The source is located at $x_1 = x_3 = 0.0$; the initial depth is 0.02 km and $\Delta x_1 = \Delta x_3 = 0.02$ km. (a) Travel-time contours by the paraxial eikonal solver with the ENO scheme. (b) The travel-time calibration at $x_3 = 1$ km.

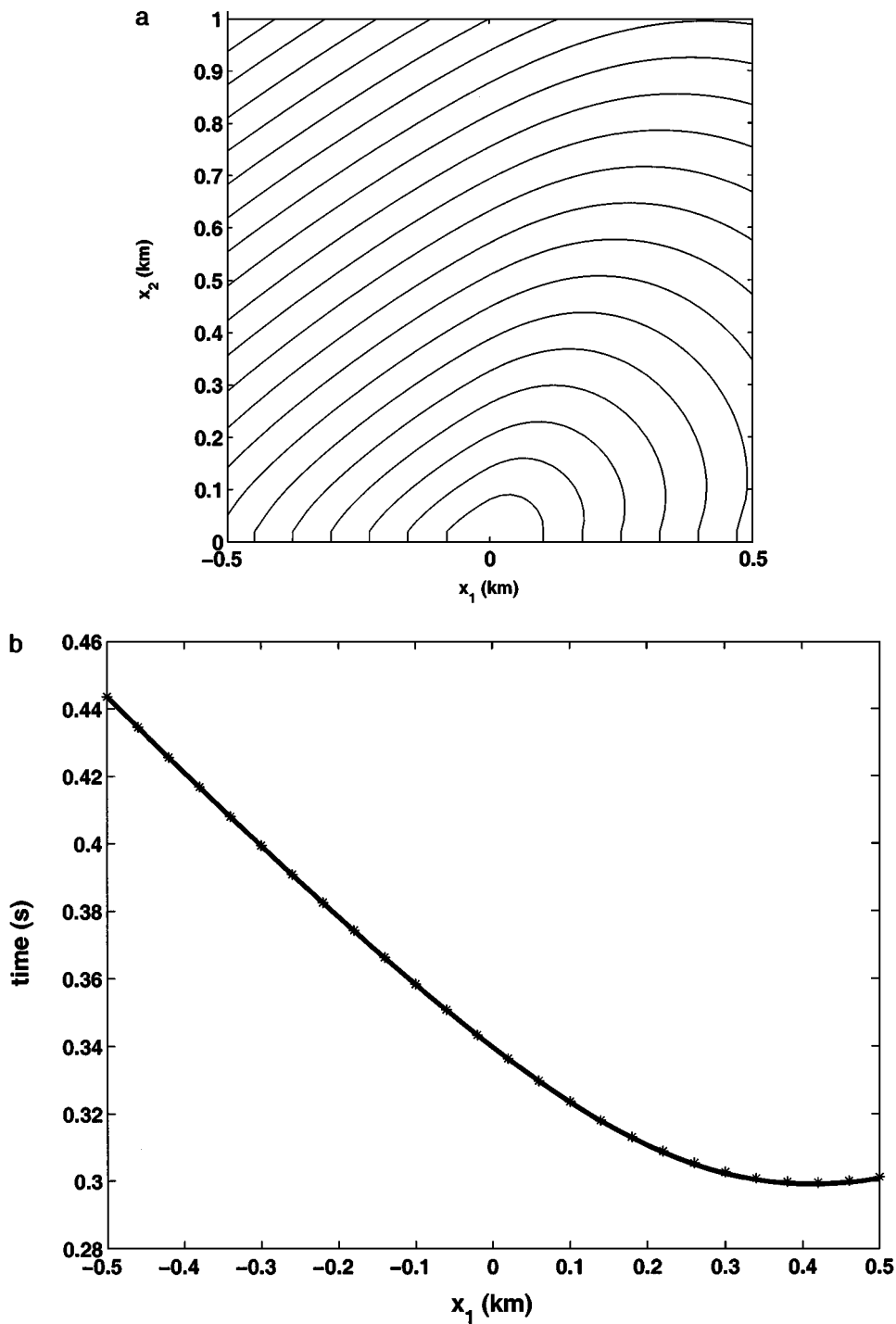


FIG. 6. The 2-D homogeneous inclined (36°) TI Zinc model with a second-order WENO scheme. The source is located at $x_1 = x_3 = 0.0$; the initial depth is 0.02 km and $\Delta x_1 = \Delta x_3 = 0.02$ km. (a) Travel-time contours by the paraxial eikonal solver with the WENO scheme. (b) The travel-time calibration at $x_3 = 1$ km.

these figures, the extreme points are located by the Newton method, and then a number of samplings are taken for p_1 in the interval (p_1^-, p_1^+) .

Figures 5 and 6 show the travel-time contours and calibrations for the two schemes. The calibrations show that the schemes work very well.

7. CONCLUSIONS

We have formulated for the heterogeneous anisotropic solids the paraxial eikonal equation satisfied by the first-arrival travel time associated with qP wave propagation. We have presented complete implementation details for computing the paraxial Hamiltonian and illustrated its application to the transversely isotropic solid. We have introduced second-order ENO/WENO schemes by using a first-order scheme presented in the Appendix as a building block. Higher order schemes may be constructed by further use of this method [36]. These schemes solve the qP paraxial eikonal equation in $O(N)$ floating point operations (where N is the number of grid points). Numerical results have shown that our scheme is accurate and efficient; for numerical results on complex models and models with both lateral and vertical variations, see [36]. The chief shortcoming is that the paraxial assumption permits us to compute travel times along down-going rays only; for example, we do not compute the overturning wavefronts. However, the paraxial formulation does provide a natural framework for performing down-and-out and postsweeping iterations [10, 20] to obtain the full aperture anisotropic travel-time field [37]. Further improvements can be made by implementing a fully adaptive eikonal solver based on a posteriori error estimates for general numerical methods for Hamilton–Jacobi equations [1].

The scheme can be used in many geoscience applications requiring modeling of anisotropic wave propagation, such as 3-D Kirchhoff migration and modeling, tomography, and 3-D controlled illumination modeling.

APPENDIX: A NEW DERIVATION OF A FIRST-ORDER GODUNOV SCHEME

In this appendix, we derive a first-order scheme from ray tracing rather than directly from the eikonal equation. Nonetheless, the end result will be recognizable as a difference approximation to the eikonal equation. We consider the two-dimensional case to illustrate the idea, which means all out-of-plane components vanish in the equations formulated for 3-D media and all rays stay in the x_1x_3 plane.

The first-order finite-difference approximation to the qP eikonal equation rests on several approximations; that is, we may approximate locally near a grid point:

1. the group velocity v_g by a constant;
2. the rays by straight line segments;
3. the travel time by piecewise linear functions of x_1 with nodes at the grid point.

Given a Cartesian grid $(m\Delta x_1, n\Delta x_3)$ in two-dimensional space, let

$$\tau_m^n \approx \tau(m\Delta x_1, n\Delta x_3) \tag{A.1}$$

be the grid function approximating the travel time. Near $(m\Delta x_1, n\Delta x_3)$, we define the

approximation of derivative τ_{x_1} at $(x_1, n\Delta x_3)$ by

$$\tau_{x_1}^n \approx \begin{cases} D_{x_1}^- \tau_m^n \equiv \frac{\tau_m^n - \tau_{m-1}^n}{\Delta x_1} & \text{for } (m-1)\Delta x_1 < x_1 < m\Delta x_1, \\ D_{x_1}^+ \tau_m^n \equiv \frac{\tau_{m+1}^n - \tau_m^n}{\Delta x_1} & \text{for } m\Delta x_1 < x_1 < (m+1)\Delta x_1. \end{cases} \tag{A.2}$$

The characteristics (rays) of eikonal equation (4) are down-going, so they can be parameterized by $x_3 = z$ and satisfy (in the two-dimensional case)

$$\frac{dx_1}{dx_3} = -\frac{\partial H}{\partial p_1}, \tag{A.3}$$

$$\frac{d\tau}{dx_3} = H - p_1 \frac{\partial H}{\partial p_1}. \tag{A.4}$$

The ray group velocity is

$$v_g = \frac{\sqrt{\left(\frac{\partial H}{\partial p_1}\right)^2 + 1}}{H(p_1) - \frac{\partial H}{\partial p_1} p_1}. \tag{A.5}$$

After discretization, the group velocity is given by

$$v_g^\pm = \frac{\sqrt{\left(\frac{\partial H}{\partial p_1}(D_{x_1}^\pm \tau_m^n)\right)^2 + 1}}{H(D_{x_1}^\pm \tau_m^n) - \frac{\partial H}{\partial p_1}(D_{x_1}^\pm \tau_m^n) D_{x_1}^\pm \tau_m^n}. \tag{A.6}$$

A ray segment passing through $(m\Delta x_1, (n+1)\Delta x_3)$ and meeting the line $x_3 = n\Delta x_3$ at x_1 has length

$$L = \Delta x_3 \sqrt{1 + \left(\frac{x_1 - m\Delta x_1}{\Delta x_3}\right)^2}, \tag{A.7}$$

so that the time predicted at $(m\Delta x_1, (n+1)\Delta x_3)$ under the foregoing assumption is

$$\tau_m^{n+1} \approx \begin{cases} \tau_m^n + (x_1 - m\Delta x_1) D_{x_1}^+ \tau_m^n + \frac{L}{v_g^+} & \text{for } m\Delta x_1 \leq x_1 \leq (m+1)\Delta x_1, \\ \tau_m^n + (x_1 - m\Delta x_1) D_{x_1}^- \tau_m^n + \frac{L}{v_g^-} & \text{for } (m-1)\Delta x_1 \leq x_1 \leq m\Delta x_1. \end{cases} \tag{A.8}$$

Finally, the ray velocity vector should obey the ray equation (A.3),

$$-\frac{x_1 - m\Delta x_1}{\Delta x_3} = \frac{dx_1}{dx_3} \approx \begin{cases} -\frac{\partial H}{\partial p_1}(D_{x_1}^+ \tau_m^n) & \text{for } m\Delta x_1 \leq x_1 \leq (m+1)\Delta x_1, \\ -\frac{\partial H}{\partial p_1}(D_{x_1}^- \tau_m^n) & \text{for } (m-1)\Delta x_1 \leq x_1 \leq m\Delta x_1, \end{cases} \tag{A.9}$$

i.e.,

$$x_1 - m\Delta x_1 \approx \begin{cases} \Delta x_3 \frac{\partial H}{\partial p_1}(D_{x_1}^+ \tau_m^n) & \text{for } m\Delta x_1 \leq x_1 \leq (m+1)\Delta x_1, \\ \Delta x_3 \frac{\partial H}{\partial p_1}(D_{x_1}^- \tau_m^n) & \text{for } (m-1)\Delta x_1 \leq x_1 \leq m\Delta x_1, \end{cases} \tag{A.10}$$

Substituting expression (A.10) into (A.8) and carrying out the algebra, we arrive at

$$\tau_m^{n+1} = \begin{cases} \tau_m^n + \Delta x_3 H(D_{x_1}^+ \tau_m^n) & \text{for } m\Delta x_1 \leq x_1 \leq (m+1)\Delta x_1, \\ \tau_m^n + \Delta x_3 H(D_{x_1}^- \tau_m^n) & \text{for } (m-1)\Delta x_1 \leq x_1 \leq m\Delta x_1, \end{cases} \quad (\text{A.11})$$

where x_1 is chosen to satisfy (A.9) if possible.

Next we have to examine the significance of the condition switching the branches of (A.11). If $m\Delta x_1 \leq x_1 \leq (m+1)\Delta x_1$, i.e., the ray slope is nonpositive, it follows from (A.9) that

$$\frac{\partial H}{\partial p_1}(D_{x_1}^+ \tau_m^n) \geq 0. \quad (\text{A.12})$$

Similarly, the second branch occurs when

$$\frac{\partial H}{\partial p_1}(D_{x_1}^- \tau_m^n) \leq 0. \quad (\text{A.13})$$

When neither of these occurs, i.e.,

$$\frac{\partial H}{\partial p_1}(D_{x_1}^+ \tau_m^n) \leq 0 \leq \frac{\partial H}{\partial p_1}(D_{x_1}^- \tau_m^n), \quad (\text{A.14})$$

rays fan away from $(m\Delta x_1, n\Delta x_3)$; that is, this point is a center of rarefaction. Then to good approximation, the ray entering $(m\Delta x_1, (n+1)\Delta x_3)$ is vertical; i.e., along it

$$\frac{\partial H}{\partial p_1} = 0, \quad (\text{A.15})$$

which corresponds to a sonic point. Finally, if both conditions are satisfied, i.e.,

$$\frac{\partial H}{\partial p_1}(D_{x_1}^+ \tau_m^n) \geq 0 \geq \frac{\partial H}{\partial p_1}(D_{x_1}^- \tau_m^n), \quad (\text{A.16})$$

then two rays converge on $(m\Delta x_1, (n+1)\Delta x_3)$, and we should select the lesser of the two times provided by (A.11).

Because the Hamiltonian H is concave, all four of these options can be combined in the simple formula

$$\tau_m^{n+1} = \tau_m^n + \Delta x_3 H^G(D_{x_1}^- \tau_m^n, D_{x_1}^+ \tau_m^n), \quad (\text{A.17})$$

where the flux H^G is defined by

$$H^G(u^-, u^+) = \begin{cases} \max_{u^- \leq u \leq u^+} H(u), & \text{if } u^- \leq u^+; \\ \min_{u^+ \leq u \leq u^-} H(u), & \text{else.} \end{cases} \quad (\text{A.18})$$

The scheme just proposed is identical to the so-called Godunov first-order scheme, and therefore it is a monotone scheme; see Osher and Sethian [30] and Osher and Shu [31].

There remains one further detail to take care of: The approximate ray might meet $x_3 = n\Delta x_3$ *outside* the interval $(m-1)\Delta x_1 \leq x_1 \leq (m+1)\Delta x_1$. The difference scheme

(A.17) would necessarily become unstable, as the numerical domain of dependence of $(m\Delta x_1, (n + 1)\Delta x_3)$ (namely, the three points on $x_3 = n\Delta x_3$ in the scheme (A.17)) would no longer contain in its convex hull the continuum domain of dependence $\{x\}$. In order to be certain this Courant-Friedrichs-Lewy (“CFL”) criterion is satisfied, we limit the slope of the ray:

$$\max \left\{ \left| \frac{\partial H}{\partial p_1}(D_{x_1}^+ \tau_m^n) \right|, \left| \frac{\partial H}{\partial p_1}(D_{x_1}^- \tau_m^n) \right| \right\} \leq \frac{\Delta x_1}{\Delta x_3}. \tag{A.19}$$

By the definition of H_Δ , for given $\Delta > 0$, there exists p'_{\max} such that [34]

$$H_\Delta(p_1) = \begin{cases} H(p_1), & \text{if } p_1 \leq (1 - \Delta)p'_{\max}, \\ H((1 - \Delta)p'_{\max}), & \text{else,} \end{cases} \tag{A.20}$$

and

$$\left| \frac{\partial H_\Delta}{\partial p_1}(p_1) \right| \leq O\left(\frac{1}{\Delta}\right). \tag{A.21}$$

Therefore, we need to choose just $\Delta > 0$ such that

$$\frac{\Delta x_1}{\Delta x_3} \geq O\left(\frac{1}{\Delta}\right). \tag{A.22}$$

Finally, the resulting difference scheme is

$$\tau_m^{n+1} = \tau_m^n + \Delta x_3 H_\Delta^G(D_{x_1}^- \tau_m^n, D_{x_1}^+ \tau_m^n), \tag{A.23}$$

which is consistent with the *paraxial eikonal equation*

$$p_3 = H_\Delta(p_1). \tag{A.24}$$

Solutions of (A.24) are identical to solutions of the eikonal equation at points whose associated rays make an angle $\leq \psi_g^{\max} = \arctan\left(\frac{\Delta x_1}{\Delta x_3}\right)$ with the vertical ($x_1 = \text{constant}$) throughout their length. (For the point source problem, the associated ray is the first-arriving ray connecting the subsurface point with the source point.) Thus with this paraxial limitation, the scheme is suitable for computing the travel time of *down-going ray fans*.

ACKNOWLEDGMENTS

The authors performed part of the research reported here while they were guests of the Stanford Exploration Project (SEP). J. Qian and W. W. Symes thank SEP members and director Professor Jon Claerbout for their hospitality and stimulating discussions. J. Qian thanks Dr. Joe Dellinger and Dr. S. Kim for helpful discussions. J. Qian also thanks the anonymous referees for their constructive comments. This work was partially supported by the National Science Foundation under Grant DMS 9627355, the Office of Naval Research under Grant N00014-96-1-0156, the U.S. Department of Energy under Grant DE-FG07-97 ER14827, and The Rice Inversion Project (TRIP). TRIP Sponsors for 1999 are Amerada Hess, Amoco Research, Conoco Inc., Exxon Production Research Co., Geophysical Development Corporation, Landmark Graphics, Mobil, and Western Geophysical.

REFERENCES

1. S. Albert, B. Cockburn, D. French, and T. Peterson, A posteriori error estimates for general numerical methods for Hamilton–Jacobi equations. I. The steady state case, *Math. Comput.* **71**, 221 (2002).
2. J.-D. Benamou, Direct solution of multi-valued phase-space solutions for Hamilton–Jacobi equations, *Commun. Pure Appl. Math.* **52**, 1443 (1999).
3. J.-D. Benamou and I. Sollic, A Eulerian method for capturing caustics, *J. Comput. Phys.* **162**, 132 (2000).
4. M. Born and E. Wolf, *Principles of Optics* (Macmillan Co., New York, 1964).
5. V. Cerveny, Seismic rays and ray intensities in inhomogeneous anisotropic media, *Geophys. J. R. Astrophys. Soc.* **29**, 1 (1972).
6. A. Cherrett and S. Singh, Travel time and polarisation tomography in 3-D anisotropic media, in *68th Annual International Meeting, Society of Exploration Geophysics*, expanded abstr. (Soc. Expl. Geophys., Tulsa, 1998), pp. 1859–1862.
7. M. G. Crandall and P. L. Lions, Viscosity solutions of Hamilton–Jacobi equations, *Trans. Am. Math. Soc.* **277**, 1 (1983).
8. M. G. Crandall and P. L. Lions, Two approximations of solutions of Hamilton–Jacobi equations, *Math. Comput.* **43**, 1 (1984).
9. J. Dellinger, *Anisotropic Seismic Wave Propagation*, Ph.D. thesis (Stanford University, 1991).
10. J. Dellinger and W. W. Symes, Anisotropic finite-difference travel times using a Hamilton–Jacobi solver, in *67th Annual International Meeting, Society of Exploration Geophysics*, expanded abstr. (Soc. Expl. Geophys., Tulsa, 1997), pp. 1786–1789.
11. D. Eaton, Finite difference travel-time calculation for anisotropic media, *Geophys. J. Int.* **114**, 273 (1993).
12. M. A. El-Mageed, S. Kim, and W. W. Symes, 3-D Kirchhoff migration using finite difference travel times and amplitudes, in *Annual Report, The Rice Inversion Project* (Rice Univ., Houston 1997), available at <http://www.trip.caam.rice.edu/>.
13. L. C. Evans, *Partial Differential Equations*, Berkeley Mathematics Lecture Notes (Univ. of California Press, Berkeley, 1994).
14. F. I. Fedorov, *Theory of Elastic Waves in Crystals* (Plenum, New York, 1968).
15. C. Hu and C. W. Shu, A discontinuous Galerkin finite element method for Hamilton–Jacobi equations, *SIAM J. Sci. Comput.* **21**, 666 (2000).
16. H. Ishii, Uniqueness of unbounded viscosity solution of Hamilton–Jacobi equations, *Indiana Univ. Math. J.* **33**, 721 (1984).
17. G. S. Jiang and D. Peng, Weighted ENO schemes for Hamilton–Jacobi equations, *SIAM J. Sci. Comput.* **21**, 2126 (2000).
18. G. S. Jiang and C. W. Shu, Efficient implementation of weighted ENO schemes, *J. Comput. Phys.* **126**, 202 (1996).
19. J. B. Keller and R. M. Lewis, Asymptotic methods for partial differential equations: The reduced wave equation and Maxwell’s equations, *Surv. Appl. Math.* **1**, 1 (1995).
20. S. Kim, Wavefronts of linear elastic waves: Local convexity and modeling, *Wave Motion* **32**, 203 (2000).
21. S. Kim and R. Cook, 3-D travel-time computation using second-order ENO schemes, *Geophysics* **64**, 1867 (1999).
22. G. Kossioris, Ch. Makridakis, and P. E. Souganidis, Finite volume schemes for Hamilton–Jacobi equations, *Numer. Math.* **83**, 427 (1999).
23. S. N. Kruzkov, Generalized solutions of Hamilton–Jacobi equations of eikonal types, I, *Math. USSR Sb.* **27**, 406 (1975).
24. A. Kurganov and E. Tadmor, New high-resolution semi-discrete central schemes for Hamilton–Jacobi equations, *J. Comput. Phys.* **160**, 720 (2000).
25. R. J. LeVeque, *Numerical Methods for Conservation Laws* (Birkhauser-Verlag, Basel, 1990).
26. C. T. Lin and E. Tadmor, High-resolution nonoscillatory central schemes for Hamilton–Jacobi equations, *SIAM J. Sci. Comput.* **21**, 2163 (2000).

27. P. L. Lions, *Generalized Solutions of Hamilton–Jacobi Equations* (Pitman, London, 1982).
28. X. D. Liu, S. J. Osher, and T. Chan, Weighted essentially nonoscillatory schemes, *J. Comput. Phys.* **115**, 200 (1994).
29. M. J. P. Musgrave, *Crystal Acoustics* (Holden–Day, Oakland, CA, 1970).
30. S. J. Osher and J. A. Sethian, Fronts propagating with curvature-dependent speed: Algorithms based on Hamilton–Jacobi formulations, *J. Comput. Phys.* **79**, 12 (1988).
31. S. J. Osher and C. W. Shu, High-order essentially nonoscillatory schemes for Hamilton–Jacobi equations, *SIAM J. Numer. Anal.* **28**, 907 (1991).
32. V. Pereyra, Two-point ray tracing in general 3-D media, *Geophys. Prospect.* **40**, 267 (1992).
33. R. Pratt and C. Chapman, Travel-time tomography in anisotropic media 4. II. Application, *Geophys. J. Int.* **109**, 20 (1992).
34. J. Qian, *Geometrical Optics for Quasi-P Waves: Theories and Numerical Methods*, Ph.D. thesis (Rice University, 2000). UMI microform 9969308.
35. J. Qian and W. W. Symes, Adaptive finite difference method for travel time and amplitude, *Geophysics*, to appear.
36. J. Qian and W. W. Symes, Finite-difference quasi-P travel times for anisotropic media, *Geophysics*, to appear.
37. J. Qian, W. W. Symes, and J. A. Dellinger, A full-aperture anisotropic eikonal solver for quasi-P travel times, Expanded abstr. submitted for publication, in *71st International Annual Meeting, Society of Exploration Geophysics*, Expanded abstr. (Soc. Expl. Geophys., Tulsa, 2001).
38. F. Qin, Y. Luo, K. B. Olsen, W. Cai, and G. T. Schuster, Finite difference solution of the eikonal equation along expanding wavefronts, *Geophysics* **57**, 478 (1992).
39. F. Qin and G. T. Schuster, First-arrival travel time calculation for anisotropic media, *Geophysics* **58**, 1349 (1993).
40. M. Reshef and D. Kosloff, Migration of common shot gathers, *Geophysics* **51**, 324 (1986).
41. W. A. Schneider Jr., Robust and efficient upwind finite-difference travel-time calculations in three dimensions, *Geophysics* **60**, 1108 (1995).
42. W. A. Schneider Jr., K. Ranzinger, A. Balch, and C. Kruse, A dynamic programming approach to first-arrival travel-time computation in media with arbitrarily distributed velocities, *Geophysics* **57**, 39 (1992).
43. J. A. Sethian and A. M. Popovici, 3-D travel-time computation using the fast marching method, *Geophysics* **64**, 516 (1999).
44. P. M. Shearer and C. H. Chapman, Ray tracing in anisotropic media with a linear gradient, *Geophys. J.* **94**, 575 (1988).
45. C. W. Shu, Essentially nonoscillatory and weighted essentially nonoscillatory schemes for hyperbolic conservation laws, in *Advanced Numerical Approximation of Nonlinear Hyperbolic Equations*, edited by A. Quarteroni, Lecture Notes in Mathematics (Springer-Verlag, Berlin, 1998), Vol. 1697, pp. 325–432.
46. W. W. Symes, R. Versteeg, A. Sei, and Q. H. Tran, Kirchhoff simulation, migration, and inversion using finite difference travel time and amplitudes, in *Annual Report, The Rice Inversion Project* (Rice Univ., Houston, 1994), available at <http://www.trip.caam.rice.edu/>.
47. L. Thomsen, Weak elastic anisotropy, *Geophysics* **51**, 1954 (1986).
48. I. Tsvankin and L. Thomsen, Inversion of reflection travel times for transverse isotropy, *Geophysics* **60**, 1095 (1995).
49. J. van Trier and W. W. Symes, Upwind finite-difference calculation of travel times, *Geophysics* **56**, 812 (1991).
50. J. Vidale, Finite-difference calculation of travel times, *Bull. Seismal. Soc. Am.* **78**, 2062 (1988).